Renewable Energy 185 (2022) 61–74

Contents lists available at ScienceDirect

Renewable Energy

journal homepage: www.elsevier.com/locate/renene

Tidal stream energy potential in the Shannon Estuary

D.M. Fouz [a], R. Carballo [a, *], I. López [a], G. Iglesias [b, c]

[a] Departamento de Enxeñaría Agroforestal, Universidade de Santiago de Compostela, EPSE, Rúa Benigno Ledo s/n, 27002, Lugo, Spain
[b] School of Engineering and Architecture & MaREI, Environmental Research Institute, University College Cork, Ireland
[c] School of Engineering, Computing and Mathematics, University of Plymouth, UK

ARTICLE INFO

Article history:
Received 14 May 2021
Received in revised form
25 November 2021
Accepted 13 December 2021
Available online 15 December 2021

Keywords:
Tidal stream energy
River in-stream energy
Non-depth-limited areas
Numerical modelling
Resource assessment

ABSTRACT

The tidal and river in-stream energy resource in the Shannon Estuary (W Ireland) is investigated using of high-resolution numerical modelling and spatial analysis. Although freshwater discharges are large, their influence on the available resource is found to be all but negligible, the tide being the main driver of estuarine circulation. The Tidal Stream Exploitability (TSE) index is adapted to the analysis of estuaries with non-depth-limited areas (TSE_{ndl}), such as the Shannon Estuary, and then used to select the hotspots with potential for a tidal stream farm. For this purpose, a new depth penalty-limiting function is defined to avoid overestimating the available energy potential in areas with depths greater than those required for tidal energy converter operation. Seven hotspots are identified based on the revised index. The approach followed in this study illustrates the applicability of high-resolution numerical modelling and spatial analysis for identifying the most appropriate areas for tidal stream energy conversion. Finally, the potential of tidal stream energy to contribute to the much-needed decarbonisation of the energy mix in Ireland is emphasized.

1. Introduction

Climate change and global warming have drawn attention to two environmental priorities of 21st century societies – greenhouse gas emissions and air pollution [1–4]. These are paramount priorities in coastal areas, where socioeconomic activity is intense, resulting in high energy consumption [5–8]. This is the case of the Shannon Estuary, the largest estuary in Ireland (Fig. 1), which harbours six commercial maritime terminals managed by the Shannon Foynes Port Company (SFPC): (from East to West) Limerick Docks, Shannon Airport, Aughinish, Port of Foynes, Tarbert and Moneypoint.

The high energy consumption in coastal areas coexists with a vast Marine Renewable Energy (MRE) resource, which emerges as a promising alternative for diversifying and decarbonising the energy supply [9–15]. In particular, tidal stream energy is significant in certain estuarine areas, mainly because it is predictable and has a relatively low environmental impact [16–22]. Its large tidal range (up to 5.5 m in spring tides, i.e., macrotidal) makes the Shannon Estuary a potential source for hydrokinetic energy conversion. The tidal regime is semidiurnal, with a form factor $F = 0.082$ [23]. The estuary tapers gradually from widths of ~15 km (water depths of ~40 m) at its mouth to less than 100 m (and water depths less than 5 m) in the inner estuary, including large intertidal areas [24].

The River Shannon, the longest in Ireland, the River Feale, and others, flow into the estuary, which has a total catchment area of 16,865 km^2 (or one sixth of the area of Ireland). Of its total length of ~400 km, ~100 km correspond to its estuary. The large river discharges may have an effect on the available resource, and as a result, on hydrokinetic energy farm operation.

This study examines the hydrokinetic (tidal and river in-stream) energy resources in the Shannon Estuary, with a focus on supplying part of the electricity demand of several coastal facilities. The first step is to accurately characterize all the tidal and river flows in the estuary. A high-resolution shallow-water numerical model is implemented to simulate the hydrodynamics. Then, the distribution of the hydrokinetic energy resource is analysed by considering different case studies. An accurate river in-stream resource characterization for this requires an intra-annual analysis of river-induced currents, including the variability of the hydrological regime of the rivers discharging into it [17,25,26].

Thus, the present study is developed by analysing different cases capturing the variability of both the tidal and river in-stream energy resource. First, four characteristic seasonal

* Corresponding author.
E-mail address: rodrigo.carballo@usc.es (R. Carballo).

https://doi.org/10.1016/j.renene.2021.12.055

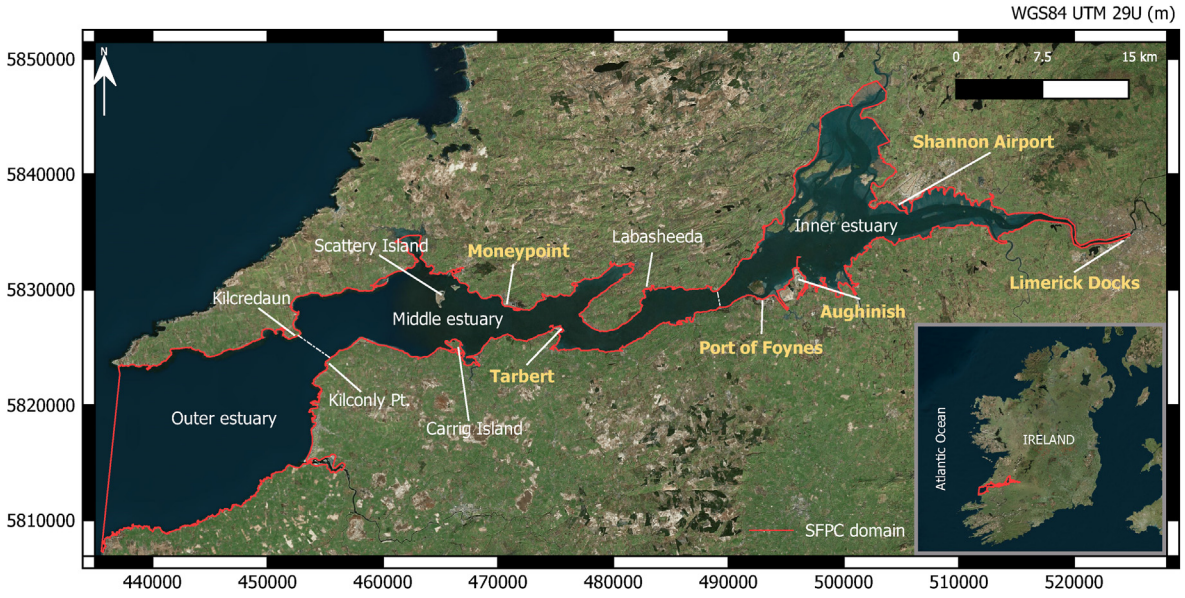

Fig. 1. Location of the Shannon Estuary, with the SFPC limits and port facilities.

scenarios are analysed for a baseline period covering a complete mean spring-neap tidal cycle and seasonal riverine discharges. The resulting dataset provides a general picture of the magnitude and distribution of the hydrokinetic energy resource, as well as the extent of riverine influx contributions to the resource. Then, a complete annual scenario is simulated for computation of the total available hydrokinetic resource. On this basis, a new ad hoc version of the Tidal Stream Exploitability (TSE) index [27] is defined for non-depth-limited estuaries (TSE_{ndl}), such as the Shannon Estuary. This new version of the index is used to select the areas of interest for hydrokinetic energy exploitation, which are then examined in greater detail. The results form the basis for a plan for hydrokinetic power supply for the Shannon Estuary facilities.

2. Materials and methods

2.1. Model implementation

A high-resolution hydrodynamic numerical model of the Shannon Estuary was implemented and validated with field data. The model, Delft3D-FLOW, is a finite-difference code that approximates the Navier-Stokes equations under the Shallow Water and Boussinesq assumptions, coupled with the transport equation, which enables the spatial distribution of the temperature, salinity, and thereby density, to be computed. Density may not be irrelevant in view of the large river inflows in this estuary. Delft3D-FLOW can be implemented either as a 3D model [28,29] or in its 2DH form (depth integrated). The 2DH form is used in this study based on previous hydrokinetic energy analyses [17,30–33]. Under these assumptions, the model equations can be expressed as [31,32,34]:

$$\frac{\partial \zeta}{\partial t}+\frac{\partial[(d+\zeta)U]}{\partial x}+\frac{\partial[(d+\zeta)V]}{\partial y}=S, \tag{1}$$

$$\left.\begin{aligned}\frac{\partial U}{\partial t}+U\frac{\partial U}{\partial x}+V\frac{\partial U}{\partial y}-fV&=-g\frac{\partial \zeta}{\partial x}-\frac{g}{\rho_0}\int_{-d}^{\zeta}\frac{\partial \rho'}{\partial x}dz+\frac{\tau_{sx}-\tau_{bx}}{\rho_0(d+\zeta)}+\upsilon_h\nabla^2 U\\ \frac{\partial U}{\partial t}+U\frac{\partial V}{\partial x}+V\frac{\partial V}{\partial y}+fU&=-g\frac{\partial \zeta}{\partial y}-\frac{g}{\rho_0}\int_{-d}^{\zeta}\frac{\partial \rho'}{\partial y}dz+\frac{\tau_{sy}-\tau_{by}}{\rho_0(d+\zeta)}+\upsilon_h\nabla^2 V\end{aligned}\right\}, \tag{2}$$

$$\frac{\partial(\zeta+d)c}{\partial t}+\frac{\partial[(\zeta+d)Uc]}{\partial x}+\frac{\partial[(\zeta+d)Vc]}{\partial y}=D_h\nabla^2 c-\lambda_d(d+\zeta)c+C, \tag{3}$$

where the conservation of mass and momentum in the x- and y-directions correspond to equations (1) and (2), respectively, and the spatial distribution of salinity and temperature (and as a result density) is computed by equation (3). In these expressions, d and ζ represent the water depth and water level, respectively; U and V are the depth-integrated velocity components in x and y directions, respectively; ρ' and ρ_0 represent the sea water anomaly and reference density, respectively; f is the Coriolis parameter; S is the source of mass; υ_h expresses the horizontal eddy viscosity; τ_{bx} and τ_{by} are the shear stress at the bottom in x and y directions; τ_{sx} and τ_{sy} represent the wind stress acting on the sea surface in x and y directions, respectively; c is any constituent (here, both salinity and temperature); D_h stands for the horizontal eddy diffusivity; C is the source term of each constituent; and finally, λ_d is first order decay.

The model grid in this application not only covers the whole Shannon Estuary but also extends to the 100 m isobath, roughly 30 km offshore, to prevent spurious numerical disturbances from affecting the area of interest. The resulting grid is composed of 69,649 cells of varying-size resolution: 100 m × 100 m resolution within the estuary, gradually increasing up to 100 × 300 m from the mouth of the estuary to the ocean boundary. Bathymetry data was obtained from the INFOMAR programme (Integrated Mapping For the Sustainable Development of Ireland's Marine Resource) [35], and supplemented with topographic data to fully describe this

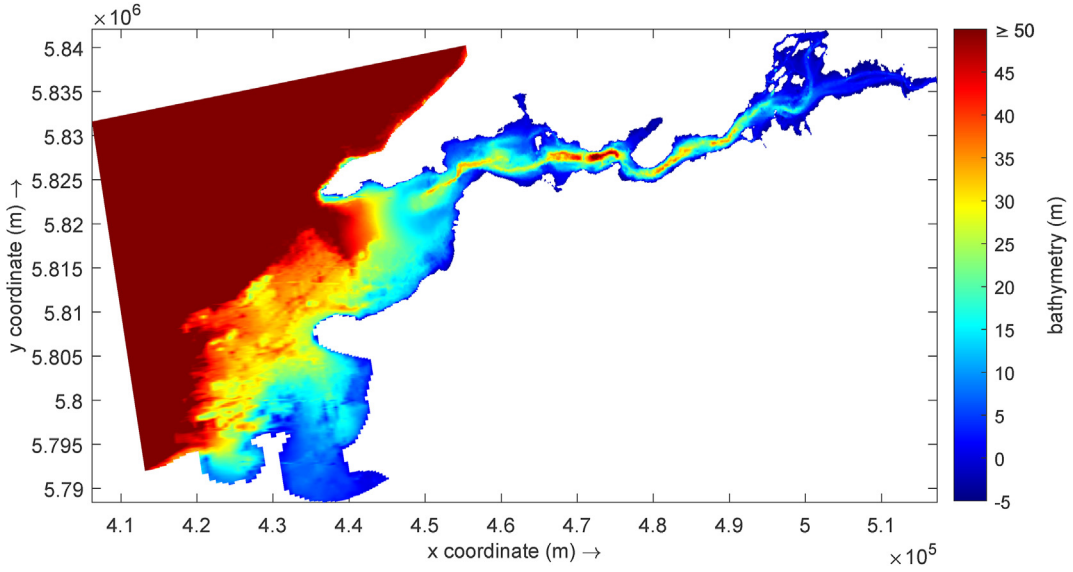

Fig. 2. Bathymetric and topographic configuration of the Shannon Estuary and its surroundings.

estuary's extensive shallows (Fig. 2).

The initial model conditions are zero free surface elevation and water velocity throughout the computational domain (*cold start*). In addition, a one-month spin-up period [36,37] is considered to ensure that the initial conditions do not affect the numerical results [26]. A Dirichlet boundary condition is applied to the open boundaries by imposing the main astronomical tidal constituents and the thermohaline conditions based on field measurements. Finally, null flow and free slip conditions (i.e., zero shear stress) are imposed on closed boundaries.

2.2. Field data and model validation

The model is forced and validated with a large set of field data. At the open boundaries the model is forced by the tide through its major harmonics, obtained from the TOPEX/Poseidon database [38,39], and by the thermohaline conditions of the oceanic water mass, using wave buoy data provided by the Irish Marine Institute (MI). As the Shannon Estuary receives large freshwater inflows, baroclinic and barotropic forcing may be significant [40]. An accurate characterization of the hydrological regime of freshwater inputs is therefore required. Freshwater inputs are obtained from gauging stations operated by the Irish Office of Public Works (OPW) which enables to include the intra-annual variability in the discharge of the most important rivers flowing into the estuary: Shannon, Fergus, Feale, Mulkear, Killimor, Deel, Maigue, Ollatrim and Killimor. The average monthly discharges of these freshwater inputs are shown in Fig. 3. Their variability can be characterized seasonally, with a rather constant contribution of the River Shannon to the total discharge (Table 1).

A second dataset for model validation consists of flow velocity field measurements as recorded by Acoustic Doppler Current Profilers (ADCP) deployed at two sites (Table 2) in the inner and middle estuary over different time periods.

ADCP measurements were taken at a sampling frequency of 30 min and 10 min at stations S1 and S2, respectively, during about one month at S1 and four days at S2. These measurements were denoised by a low-pass filter designed ad hoc [41] and vertically averaged for comparison with model results.

Fig. 4 shows a comparison of the magnitude of flow velocity computed by the model to measured data from S1 and S2. Overall, the agreement is excellent, with coefficients of determination, R^2, of 0.81 and 0.92, and root mean square errors, RMSE, of 0.211 and

Table 1
Seasonal variability of freshwater inputs to the Shannon Estuary.

Season	Total river discharge (m^3s^{-1})	Contribution of River Shannon (%)
Winter	668.14	75
Spring	501.24	86
Summer	334.16	79
Autumn	390.70	68

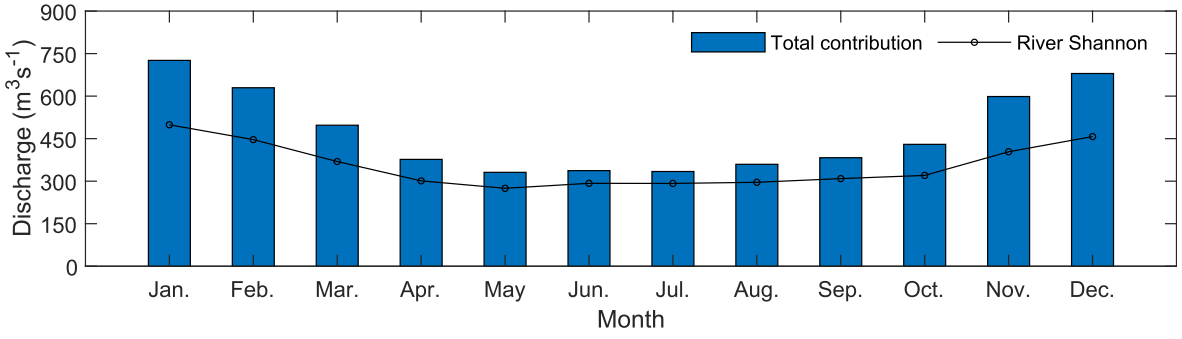

Fig. 3. Total monthly freshwater inputs in the Shannon estuary (blue bars) and contribution of the River Shannon (black line).

Table 2
Location of deployment points for ADCP.

Location	ID	X-Coordinate (m) WGS84 UTM 29U	Y-Coordinate (m) WGS84 UTM 29U	Water depth (m) low tide
Scattery Island	S1	464655	5827265	14.0
River Fergus	S2	500607	5836220	10.0

0.079 ms^{-1}, for S1 and S2, respectively, showing that the model can accurately predict the hydrodynamics of this estuary.

2.3. Spatial analysis of the TSE_{ndl} index

The Tidal Stream Exploitability (TSE) index was designed for tidal stream energy conversion site selection in areas with limited water depth [27]. It may be expressed as:

$$TSE = \frac{\xi}{2V_0^3 h_0}\left(V_f^3 + V_e^3\right)h, \tag{4}$$

where V_0 and h_0 represent the characteristic velocity and characteristic water depth, respectively, which are usually set as 1.5 ms^{-1} (V_0) and 5 m (h_0); V_f and V_e are the average velocities at mid-flood and mid-ebb, respectively; h is the water depth at mid-tide; finally, ξ is a penalty function which depends on the water depth and computed as:

$$\xi = \begin{cases} 0,\ h - \dfrac{\Delta h}{2} \le h_1 \\ \dfrac{1}{h_2 - h_1}\left(h - \dfrac{\Delta h}{2} - h_1\right),\ h_1 < h - \dfrac{\Delta h}{2} < h_2 \\ 1,\ h - \dfrac{\Delta h}{2} \ge h_2 \end{cases}, \tag{5}$$

where Δh is the maximum tidal range in the study area; h_1 and h_2 represent the lower and upper limits of the depth penalty range, usually set as 2 m (h_1) and 5 m (h_2), respectively. For further information on the TSE index, see Ref. [27].

As the TSE index was designed for shallow and intermediate water depths, where the depth is a major constraint for the selection of potential tidal stream energy conversion sites [27,32,42,43], it should be modified for its application to deep estuaries, such as the Shannon Estuary, where depth does not have the same role. In this work, a new version of this index adapted to non-depth-limited estuaries, TSE_{ndl}, is proposed (Eq. (6)). To this end, the analysis of the areas with water depths over a given threshold depth is analysed by considering an additional resource-limiting expression in the above penalty function, leading to the new penalty-limiting function, ξ_{ndl} (Eq. (7)). The objective of this new function is not to overestimate the energy potential of areas with large water depths and, more specifically, areas with depths in excess than those required for the operation of the majority of Tidal Energy Converters (TECs). This is done by considering a new range in the function, given by the threshold h_3, above which TSE_{ndl} values are limited to those corresponding to water depths of h_3.

$$TSE_{ndl} = \frac{\xi_{ndl}}{2V_0^3 h_0}\left(V_f^3 + V_e^3\right)h\,, \tag{6}$$

$$\xi_{ndl} = \begin{cases} 0,\ h - \dfrac{\Delta h}{2} \le h_1 \\ \dfrac{1}{h_2 - h_1}\left(h - \dfrac{\Delta h}{2} - h_1\right),\ h_1 < h - \dfrac{\Delta h}{2} < h_2 \\ 1,\ h_2 \le h - \dfrac{\Delta h}{2} < h_3 \\ \dfrac{1}{h}\left(h_3 + \dfrac{\Delta h}{2}\right),\ h - \dfrac{\Delta h}{2} \ge h_3 \end{cases}. \tag{7}$$

Based on the characteristics of current available commercial technologies, $h_3 = 16$ m [44–46]. It is worth of mentioning that the bounds h_1, h_2 and h_3 are strongly dependent on the maturity of energy conversion systems and could therefore be adapted to future developments.

The TSE_{ndl} index is computed based on the information from the numerical model and analysed through spatial analysis [47,48], leading to the delimitation of the most suitable areas for hydrokinetic energy exploitation. This is done by physical interpretation of the TSE_{ndl} index thresholds as follows. A $TSE_{ndl} = 1$ means that the average available tidal stream power at mid-ebb and mid-flood at a given location corresponds to a tidal current with characteristic velocity ($V_0 = 1.5$ ms^{-1}) in a characteristic water depth ($h_0 = 5$ m). Thus, and based on [49,50], it can be established that TSE_{ndl} over 1 indicates locations of interest for tidal stream energy conversion, and over 2 are of high interest. These thresholds are retained for analysis in Section 4.

2.4. Case studies

The hydrokinetic energy potential of the Shannon Estuary is assessed, and thereby identified the best areas for its conversion, by analysing a number of case studies. First, a preliminary analysis is made of the distribution of the available resource considering both tide and river discharges (in addition to the thermohaline conditions at the open boundaries and resulting baroclinic flows) for a complete mean spring-neap tidal cycle (≈14.75 days). Seasonal river discharges (Fig. 3) during this period are used to define four case studies: winter (CS1), spring (CS2), summer (CS3), autumn (CS4). Once the general resource distribution has been analysed, the combined effects of the interaction of both energy resources are assessed over a long period (a complete year) (CS5) to accurately determine the total available energy. Average monthly river discharges (Fig. 3) are input to the model to this end. Even though the above information would have been sufficient to identify the areas with the largest energy resource, the most suitable areas for its conversion also depend on other variables, such as the magnitude of peak velocities or water depth. Thus, the TSE_{ndl} index is computed for a tidal cycle during spring tides and mean river discharges and thermohaline conditions (CS6). Several large areas of interest (hotspots) are delimited based on the results. This delimitation is defined by establishing the TSE_{ndl} thresholds defined in Section 2.3. Within each of these large areas, two locations are

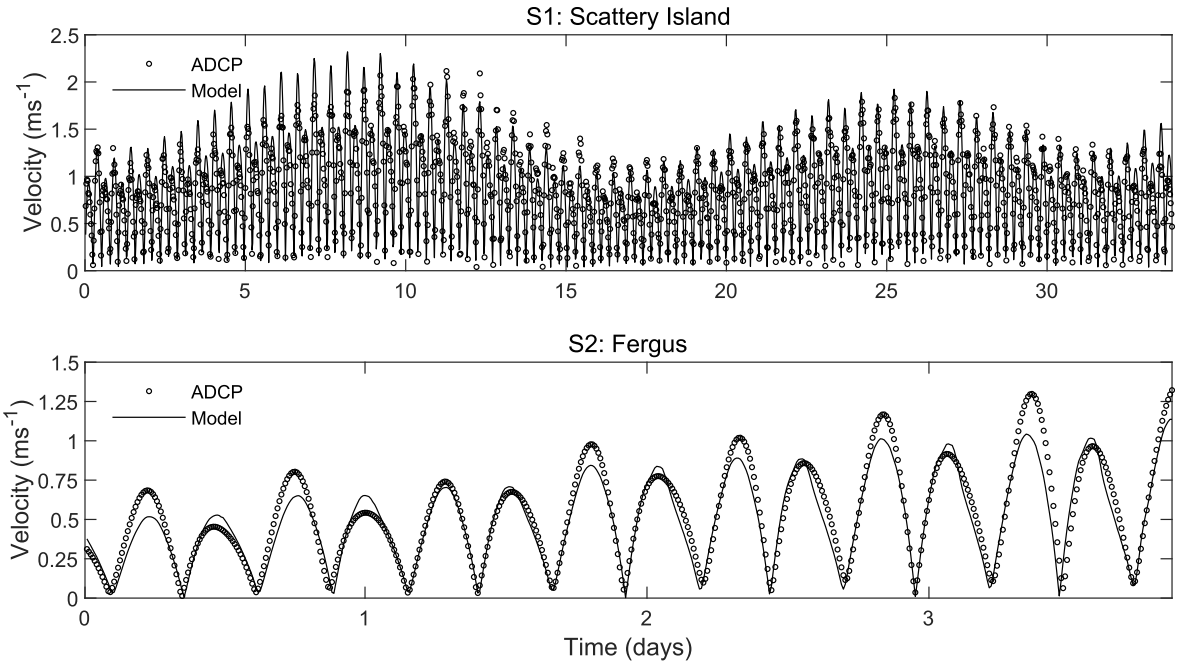

Fig. 4. Comparison of the flow velocity from numerical modelling and ADCP measurements at S1 and S2.

selected for high-resolution analysis, one with the highest TSE_{ndl}, and a representative location with the mean TSE_{ndl} for the area.

Finally, the time distribution of the available resource is analysed at the selected locations for a complete mean spring-neap tidal cycle under mean river discharges and thermohaline conditions (CS7).

3. General resource distribution

Following the procedure described in Section 2, the results of the general spatial distribution of the available resource obtained from the simulations corresponding to case studies CS1-CS4 are analysed. A preliminary key point is to investigate for the first time the influence of the freshwater inputs on the total available resource. Having analysed the large amount of information obtained, the spatial distribution of the flow field is presented at mid-ebb and mid-flood of a mean spring tide only for CS1 (winter) and CS3 (summer) for the sake of clarity (Fig. 5 and Fig. 6). These are the case studies corresponding to the seasons with the largest and least freshwater inputs.

The maximum current speeds occur in the surroundings of Tarbert, with values of up to 2.30 ms^{-1} and 1.96 ms^{-1} at mid-ebb and mid-flood, respectively, during the winter season (Fig. 5). Nevertheless, the greater fluvial discharges in winter are not capable of significantly modifying the general resource distribution, as it is apparent from the comparison between Fig. 5 (winter or CS1) and Fig. 6 (summer or CS3). The results for autumn and spring present virtually identical flow patterns and, therefore, are omitted.

In addition to the surroundings of Tarbert, there exist other areas with high current velocities that could be of interest for distributed energy generation across the estuary: the surroundings of Kilcredaun, close to the mouth, with velocities of 1.88 ms^{-1} and 1.45 ms^{-1} at mid-ebb and mid-flood, respectively; the constriction between Scattery Island and Carrig Island, in the middle estuary, with similar figures (2.08 ms^{-1} and 1.45 ms^{-1} at mid-ebb and mid-flood, respectively). Other areas of interest, with somewhat lower velocities, are the surroundings of Moneypoint (with velocities of 1.36 ms^{-1} and 1.21 ms^{-1} at mid-ebb and mid-flood, respectively) and the area close to the Port of Foynes and Aughinish (1.41 ms^{-1} and 1.11 ms^{-1} at mid-ebb and mid-flood, respectively). These areas might be of interest with a view to the energetic supply of the nearby SFPC facilities.

Based on the previous results, a clear ebb dominance [51] is apparent, probably as a result of the complex interaction of the tide with the bottom contours. This effect is complemented by the river discharges in specific areas of the inner estuary – even though their influence on the general circulation patterns is more limited than might have been expected a priori.

In order to have a more detailed knowledge of the distribution of the available resource, the results of CS5, a numerical simulation of a complete year considering the intra-annual variability of the river inputs in terms of monthly discharges, are used to accurately compute the spatial distribution of the mean power density (Fig. 7).

The areas with the greatest values of mean power density correspond to those with maximum velocities – the Tarbert area, with approx. 1.84 kWm^{-2}, followed by the channel between Scattery Island and Carrig Island, and Kilcredaun area, with 1.23 and 1.05 kWm^{-2}, respectively; and finally, the surroundings of Port of Foynes and Aughinish, and Moneypoint with 0.46 and 0.44 kWm^{-2}, respectively.

4. Selection of areas based on TSE_{ndl} index

The available energy resource in terms of power density provides valuable information for pinpointing the areas of interest for hydrokinetic energy exploitation. Nevertheless, there exist other factors which affect the operation of a hydrokinetic farm, such as the available water depth. With this in view, in order to have a clearer understanding of the exploitable resource, the spatial distribution of the TSE_{ndl} index is computed as defined in Section 2 (CS6) (Fig. 8 and Fig. 9).

The results of the TSE_{ndl} index follow a rather similar spatial distribution pattern to that provided by the power density

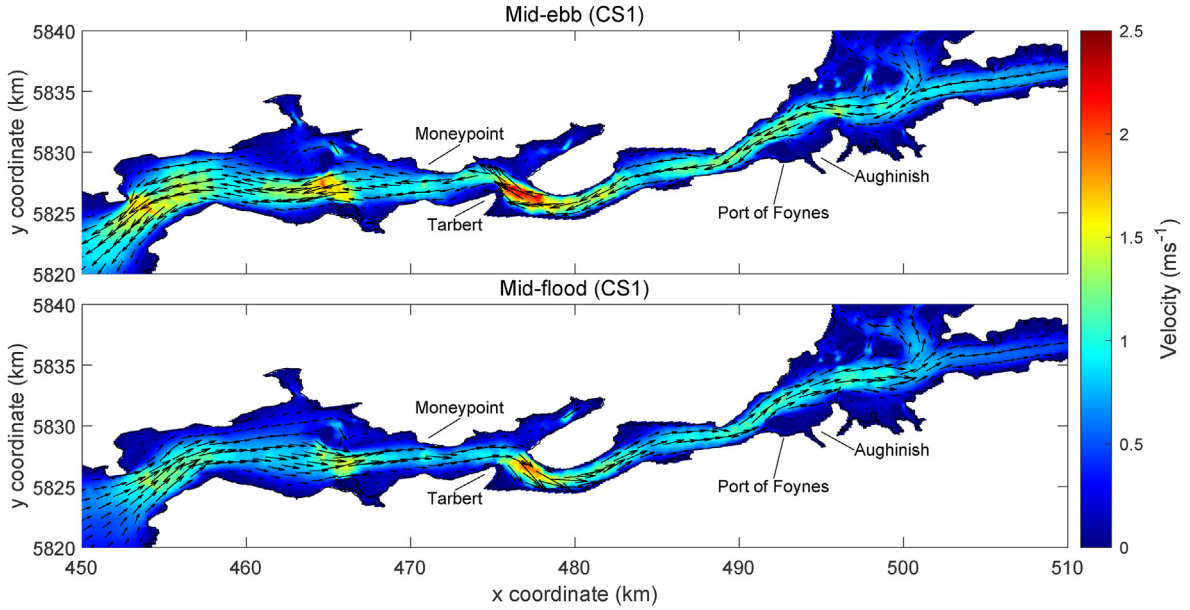

Fig. 5. Flow pattern at mid-ebb (top) and mid-flood (bottom) in CS1 (winter).

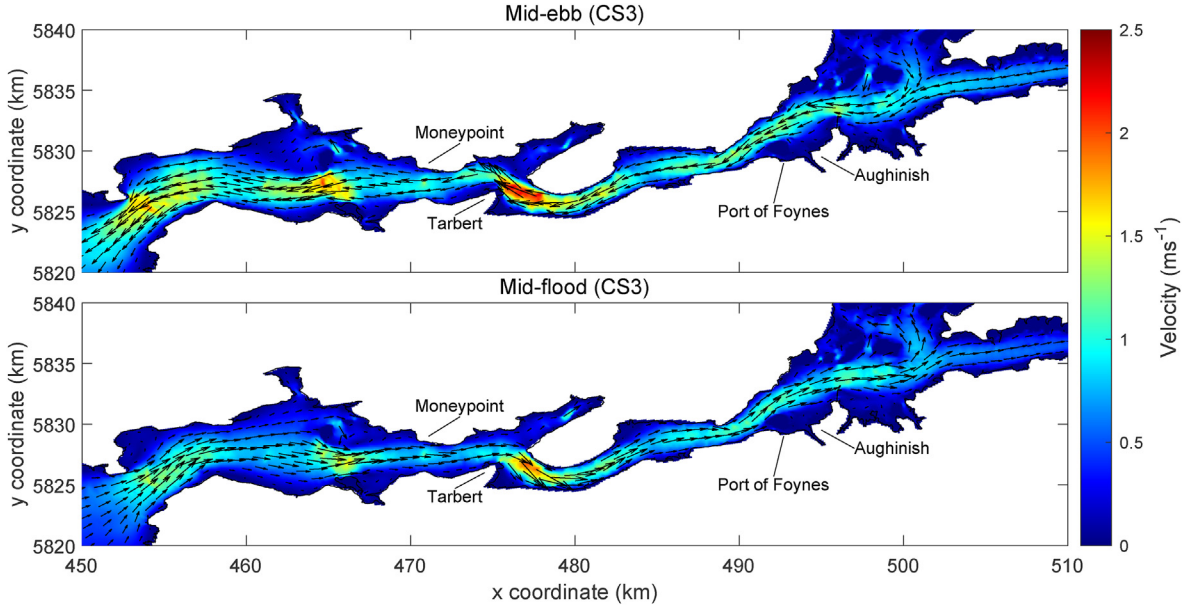

Fig. 6. Flow pattern at mid-ebb (top) and mid-flood (bottom) in CS3 (summer).

distribution. The greatest figures occur close to Tarbert, 9.36, followed, in the middle and outer estuary, by the surroundings of Kilcredaun, with 5.70, the channel between Scattery Island and Carrig Island with 5.50, and the surroundings of Moneypoint with 2.50. In the case of the inner part of the estuary, the TSE_{ndl} values range between minimums of 1.10 and maximums of 2.80 (in some specific zones) over a large area, which roughly corresponds to the central channel, attaining 2.1 close to the Port of Foynes and Aughinish.

Having analysed the spatial distribution of the TSE_{ndl} index, it emerges that extensive areas may be suitable for hydrokinetic energy exploitation. However, the installation of a hydrokinetic farm requires the accurate delimitation of the areas suited for its operation. To this end, following the approach described in Section 2, the values of the TSE_{ndl} index are analysed by applying spatial analysis techniques. More specifically, the areas above two thresholds of TSE_{ndl} ($TSE_{ndl} = 1$ and $TSE_{ndl} = 2$) are delimited (Figs. 9 and 10).

The resulting areas are plotted in Fig. 9. A total of seven areas (Area I to VII) are identified in the Shannon Estuary, whose main characteristics are provided in Table 3.

The results show that all the identified areas are of interest for hydrokinetic energy exploitation, in particular areas I, II and IV. However, areas I and II are far away from SFPC facilities. Nearer to SFPC facilities, but with a somewhat lower resource, are: Area III (close to Moneypoint), Area VI (close to the Port of Foynes) and Area VII (near Aughinish). On this basis, Areas III, IV, VI and VII are retained for further analysis in the following section.

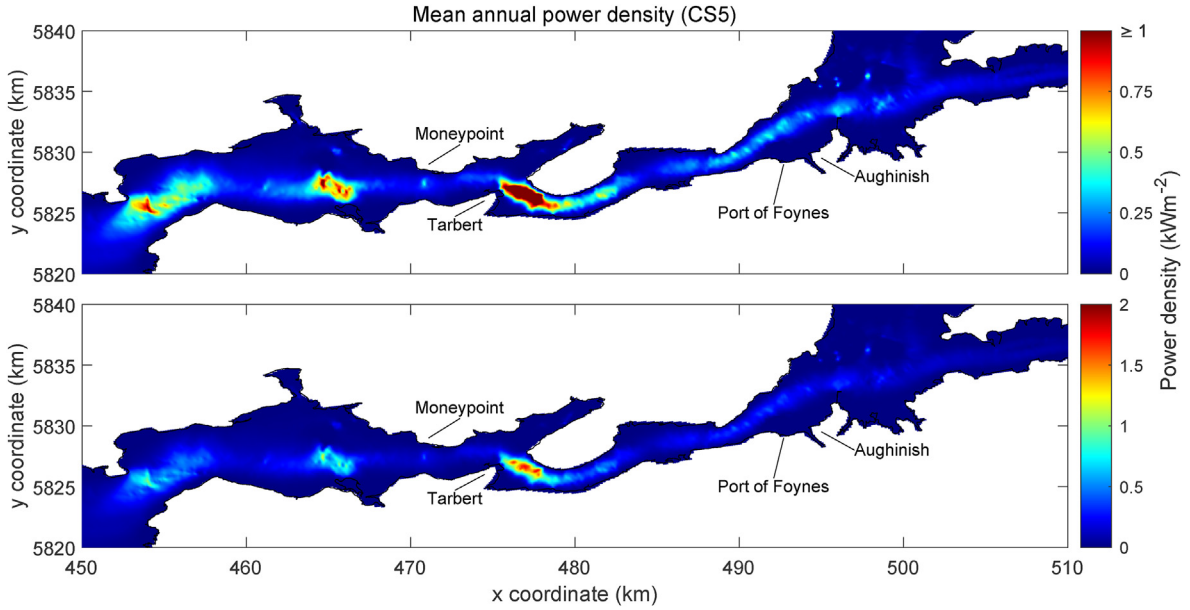

Fig. 7. Spatial distribution of the mean annual power density as obtained from CS5. The colour scale is adapted to appropriately describe the power density distribution throughout the estuary (top) and the maximum values attained (bottom).

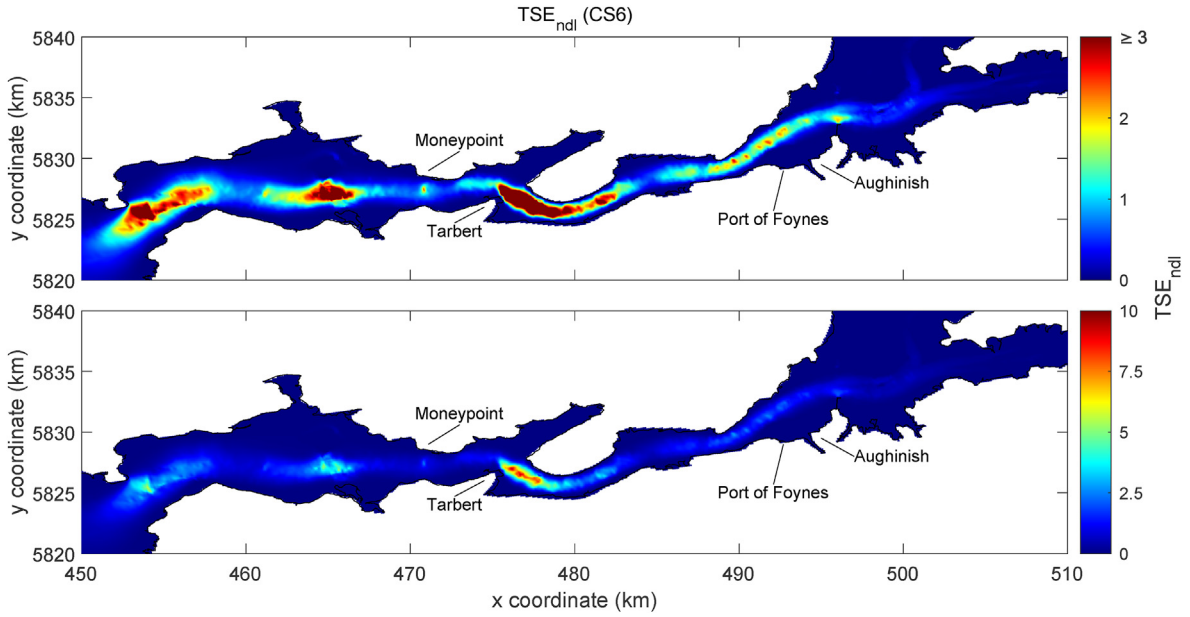

Fig. 8. Spatial distribution of the TSE_{ndl} as obtained from CS6. The colour scale is adapted to appropriately describe the TSE_{ndl} distribution throughout the estuary (top) and the maximum values attained (bottom).

5. High-resolution spatiotemporal analysis of the selected areas

In this section, in order to provide further information of interest for the operation of a tidal energy farm within the previously selected areas (III, IV, VI and VII), their analysis is conducted by focusing on two representative locations which correspond to: (i) the mean value of the TSE_{ndl} within the delimited areas, or $L_{mean,i}$, and (ii) the maximum value of the TSE_{ndl} within the delimited areas, or $L_{max,i}$, with the index *i* denoting the Area (III, IV, VI or VII).The selected locations are pinpointed in Fig. 10.

At the selected points, the time distribution of the current velocity and power density are analysed throughout a 14.75-day mean spring-neap tidal cycle under mean river discharge (CS7) (Fig. 11–14).

In Area III, mean and peak values of the current velocity of

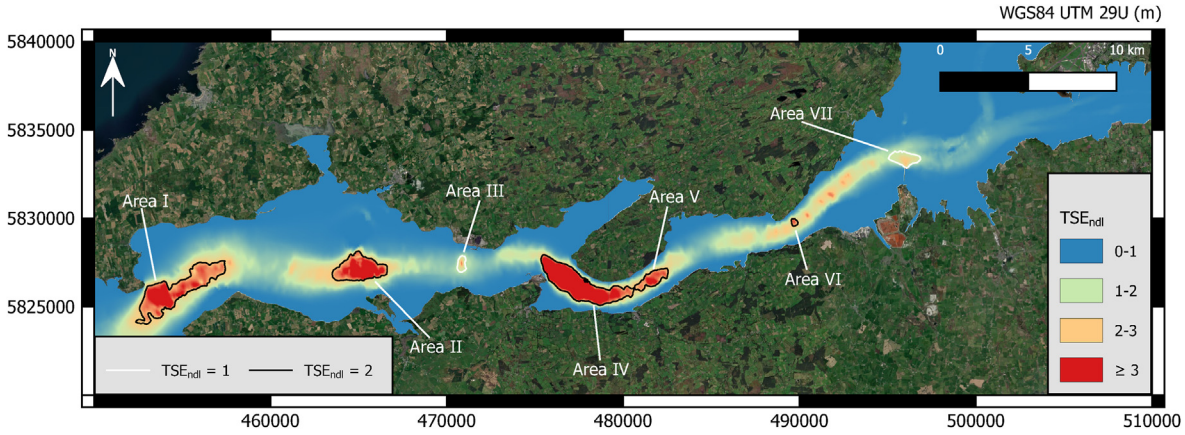

Fig. 9. Delimitation of the areas of interest for hydrokinetic energy exploitation based on the TSE_{ndl}. The lines corresponding to TSE_{ndl} values of 2 and 1 delimit the areas exceeding these thresholds.

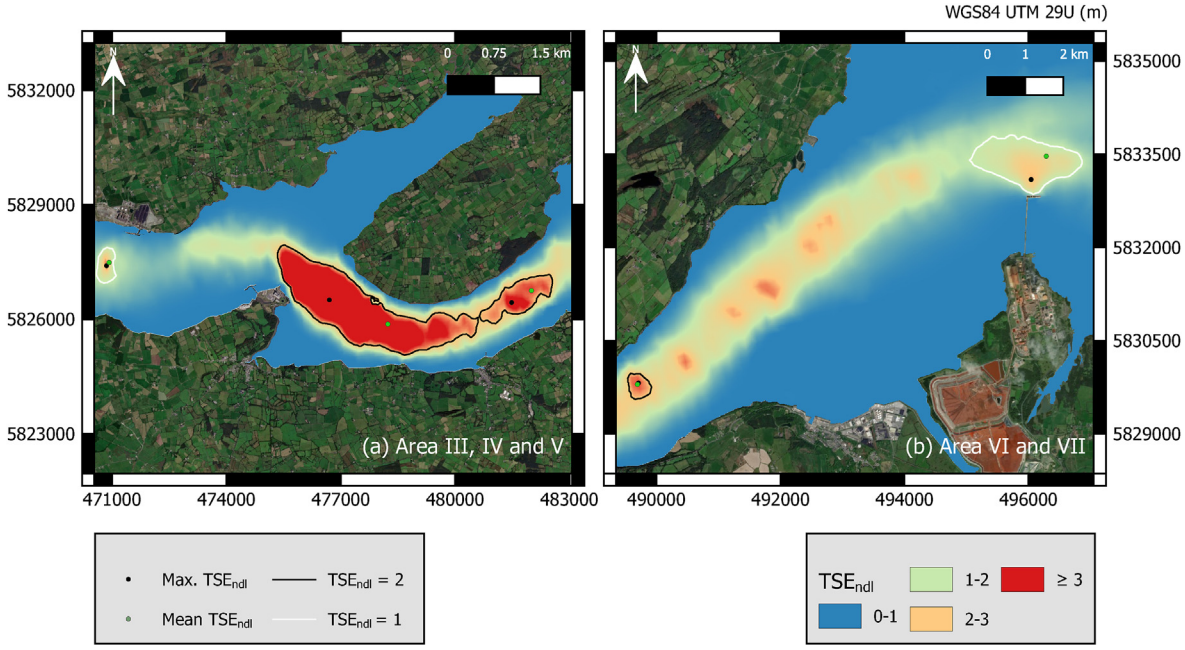

Fig. 10. Detailed view of the selected areas, identifying the representative points (maximum TSE_{ndl} and mean TSE_{ndl}) selected for high-resolution analysis.

Table 3
Main characteristics of hydrokinetic selected sites.

Area	Surface (km^2)	Mean water depth (m)	Mean TSE_{ndl}	Maximum TSE_{ndl}
I	6.1	23.0	2.7	5.7
II	3.3	17.4	3.0	5.5
III	0.4	26.4	1.4	2.5
IV	5.7	18.7	4.4	9.4
V	1.1	30.0	2.5	3.7
VI	0.1	23.2	2.3	2.8
VII	1.0	12.6	1.4	2.1

0.61 ms^{-1} and 1.17 ms^{-1}, respectively, are attained at $L_{mean,III}$, with somewhat larger figures at $L_{max,III}$, 0.71 ms^{-1} and 1.37 ms^{-1}, respectively. There exist significant differences between the *x*- and *y*-direction velocities, with the latter presenting much weaker values, which shows how the geographical configuration of the middle estuary influences its hydrodynamics, and therefore the most likely configuration of a hydrokinetic energy farm in this area. With respect to the power density, as expected, the differences between locations are more apparent than in the case of the velocity magnitude, with average and peak values of 0.20 kWm^{-2} and 0.82 kWm^{-2}, respectively at $L_{mean,III,}$ and 0.31 kWm^{-2} and 1.30 kWm^{-2} at $L_{max,III}$.

As for Area IV, mean and maximum values of flow magnitude of 1.06 ms^{-1} and 2.04 ms^{-1}, respectively, are present at $L_{mean,IV}$, which are again similar to those at $L_{max,IV}$, 1.14 ms^{-1} and 2.21 ms^{-1}. The *x*-direction flow remains stronger, but less so than in Area III. Both sites provide similar figures of power density, with mean values of 1.03 kWm^{-2} and 1.28 kWm^{-2}, and peak values of 4.28 kWm^{-2} and 5.49 kWm^{-2} at $L_{mean,IV}$ and $L_{max,IV}$, respectively.

In the case of Area VI, the flow field of the central channel in the middle-inner estuary up to Aughinish does not present marked spatial variations. This feature, together with the relatively reduced surface of this area (with roughly 12 hm^2 above $TSE_{ndl} = 2$), results

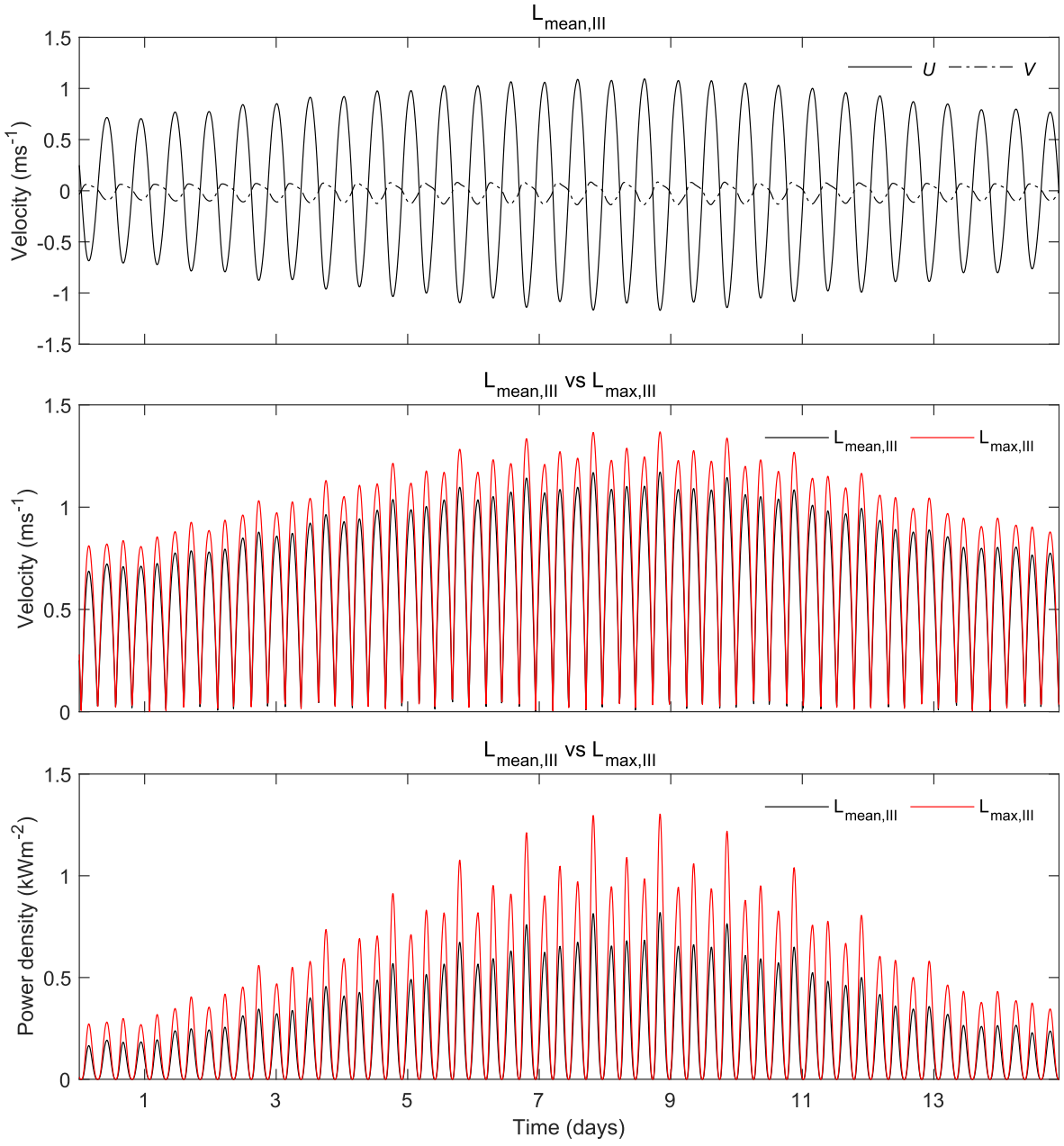

Fig. 11. High-resolution analysis in Area III showing the time distribution of the current velocity components, *U* and *V*, at $L_{mean,III}$ (above), the magnitude of current velocity at $L_{mean,III}$ and $L_{max,III}$ (intermediate), and the power density at $L_{mean,III}$ and $L_{max,III}$ (bottom).

in similar figures at both representative points, $L_{mean,VI}$ and $L_{max,VI}$, with mean current speeds of 0.69 and 0.71 ms^{-1}, and peak values of 1.41 and 1.45 ms^{-1}, respectively. The power density available at both locations is therefore similar, with mean values of 0.28 and 0.32 kWm^{-2} and maximum values of 1.41 and 1.54 kWm^{-2} at $L_{mean,VI}$ and $L_{max,VI}$, respectively.

Finally, in the uppermost area, Area VII, the mean magnitude of the current velocity at both representative locations is again similar, of 0.62 ms^{-1} at $L_{mean,VII}$ and 0.64 ms^{-1} at $L_{max,VII}$. In the case of the peak values, the differences are more apparent, with values of 1.13 ms^{-1} and 1.39 ms^{-1}, respectively. In addition, the change in the alignment of the main axis of the estuary in this area causes the *y*-axis velocity component to all but vanish. Regarding the power density, similar average values are obtained at both locations, with 0.20 kWm^{-2} at $L_{mean,VII}$ and 0.24 kWm^{-2} at $L_{max,VII}$, with much larger differences however in the maximum values, 0.74 kWm^{-2} and 1.37 kWm^{-2}, respectively.

For the sake of clarity, the previous results are summarized in Table 4, in which the values of the mean and peak velocities and power density for the period analysed at the selected locations are provided.

6. Conclusions

This study used a high-resolution analysis to characterize the tidal and river in-stream energy resource throughout the Shannon Estuary to identify the most suitable areas for its conversion. The resource is examined in a number of case studies (CS1 to CS7)

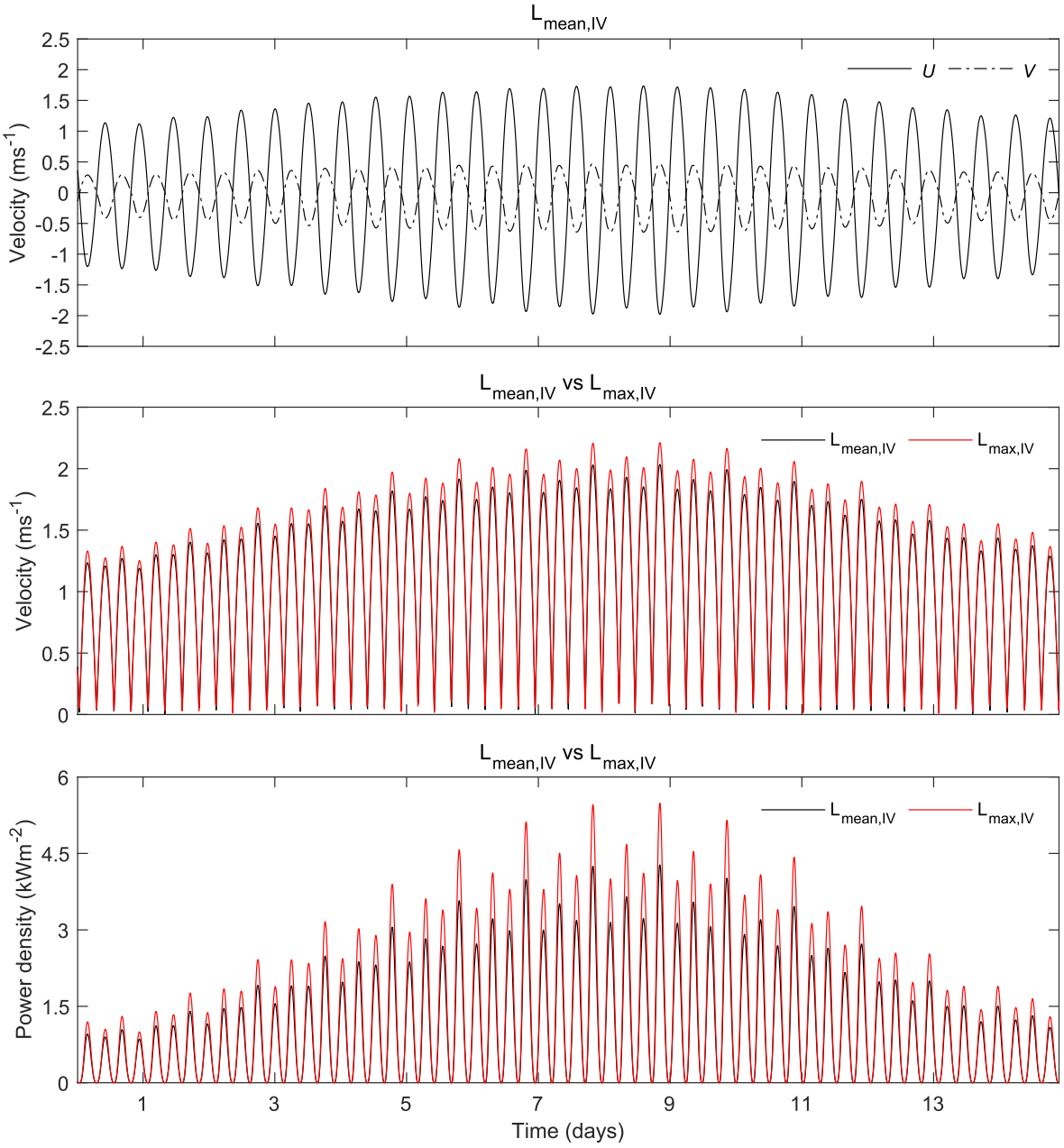

Fig. 12. High-resolution analysis in Area IV showing the time distribution of the current velocity components, *U* and *V*, at $L_{mean,IV}$ (above), the magnitude of current velocity at $L_{mean,IV}$ and $L_{max,IV}$ (intermediate), and the power density at $L_{mean,IV}$ and $L_{max,IV}$ (bottom).

through state-of-the-art numerical modelling. The model is validated against field measurements.

The hydrodynamics of the estuary are characterized in cases CS1 to CS4 which found freshwater inflows to have little influence —the Shannon Estuary is indeed tide-dominated, as a result of its large tidal range and tidal prism. In terms of hydrokinetic energy availability, the intra-annual variability that might arise from variations in freshwater discharges is all but negligible— a positive effect insofar as it would ensure seasonally stable energy production throughout the year.

The strongest current velocities are found in the Tarbert area, with peaks of up to 2.3 ms^{-1} during the ebb tide. Other hotspots are: the area surrounding Kilcredaun and the strait between Scattery Island and Carrig Island, with speeds of up to ~2 ms^{-1}. Other areas with a somewhat lower resource may be of interest given their proximity to port facilities, such as: the areas around Moneypoint and close to the Port of Foynes, and Aughinish, where speeds are ~1.4 ms^{-1}.

In Case Study CS5 an accurate estimation of the total available energy is computed by simulating a complete year under real conditions. The areas with the highest power density correspond to the strongest flows, especially, the Tarbert area, with ~2 kWm^{-2}, followed by the other hotspots, with ~1.2 kWm^{-2} to ~0.5 kWm^{-2}.

Despite the importance of the resource, the selection of hotspots for hydrokinetic energy conversion should also consider other aspects, such as the water depth, which may have an important role in the Shannon Estuary, not only because of its large areas of shallow and intermediate depths, but also deep areas. With this in

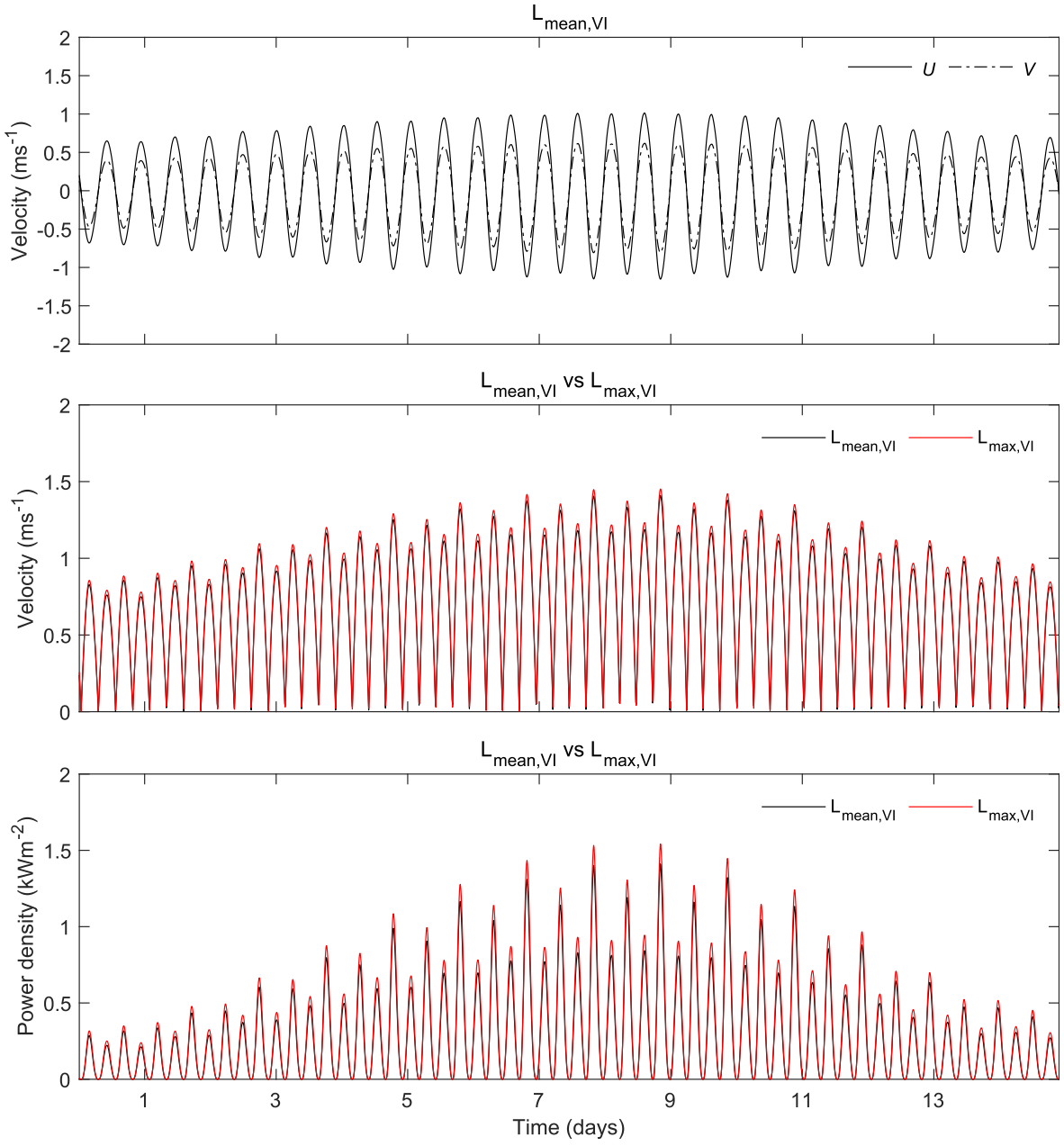

Fig. 13. High-resolution analysis in Area VI showing the time distribution of the current velocity components, *U* and *V*, at $L_{mean,VI}$ (above), the magnitude of current velocity at $L_{mean,VI}$ and $L_{max,VI}$ (intermediate), and the power density at $L_{mean,VI}$ and $L_{max,VI}$ (bottom).

view, a new version of the Tidal Stream Exploitability (TSE) index adapted to non-depth-limited areas, the TSE_{ndl} index, is proposed and implemented in Case Study CS6. A new penalty-limiting function, ξ_{ndl}, is defined for this to avoid overestimating the available tidal stream power in areas where water depths exceed than those required for operating most commercial TECs.

Seven suitable areas (I to VII) are delimited by considering specific thresholds of the TSE_{ndl} index, based on its physical meaning, and applying spatial analysis. With a view to supplying energy to the port facilities in the estuary, the distance to these facilities is also considered, resulting in the selection of four areas: III, IV, VI and VII.

Finally, a high-resolution analysis of the resource in these four areas is carried out in Case Study CS7. Two representative locations were selected in each area, corresponding to the mean and maximum TSE_{ndl} in the area. The available resource is found to differ greatly amongst areas, depending on their location within the estuary. In all four areas, there is little spatial variations in the resource, except for Area IV (Tarbert), where the TSE_{ndl} index varies from 2 to 9.36 —the reason being its large surface area.

Summarizing, the most suitable areas for tidal stream energy conversion in the Shannon Estuary were identified, and their resource characterized. The procedure implemented in this study, and in particular, the new TSE_{ndl} index, could be applied to any other coastal region of interest, including deep-water areas. The final decision regarding the installation of a hydrokinetic energy farm should consider not only the resource, but also Marine Spatial Planning, environmental and socioeconomic factors (including the

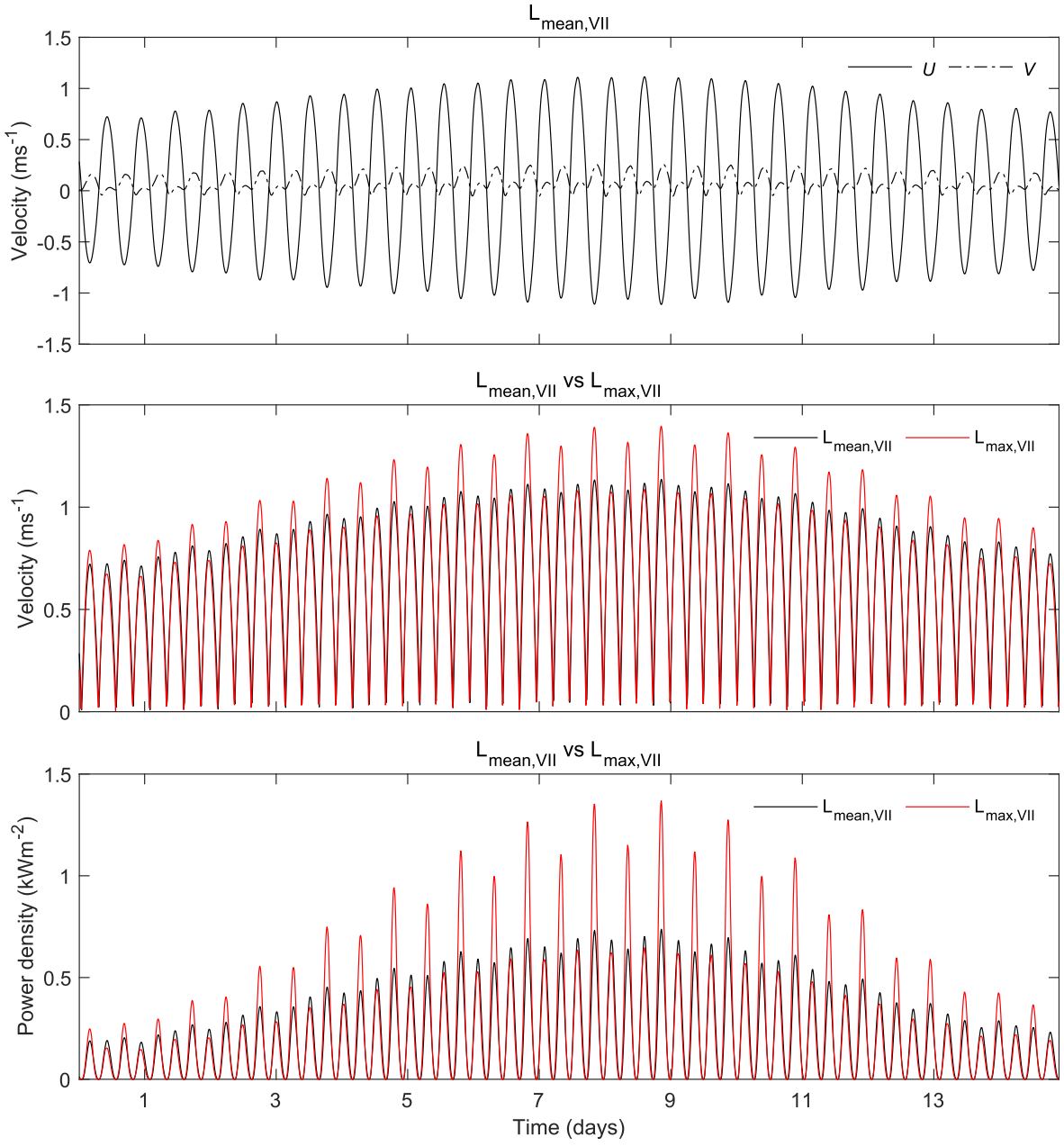

Fig. 14. High-resolution analysis in Area VII showing the time distribution of the current velocity components, *U* and *V*, at $L_{mean,VII}$ (above), the magnitude of current velocity at $L_{mean,VII}$ and $L_{max,VII}$ (intermediate), and the power density at $L_{mean,VII}$ and $L_{max,VII}$ (bottom).

Table 4
Mean and peak velocities and power density at the selected locations (CS7).

Locations	Mean velocity (ms^{-1})	Peak velocity (ms^{-1})	Mean power density (kWm^{-2})	Peak power density (kWm^{-2})
$L_{mean,III}$	0.61	1.17	0.20	0.82
$L_{max,III}$	0.71	1.37	0.31	1.30
$L_{mean,IV}$	1.06	2.04	1.03	1.28
$L_{max,IV}$	1.14	2.21	4.28	5.49
$L_{mean,VI}$	0.69	0.71	0.28	0.32
$L_{max,VI}$	1.41	1.45	1.41	1.54
$L_{mean,VII}$	0.62	0.64	0.20	0.24
$L_{max,VII}$	1.13	1.39	0.74	1.37

computation of capital and operational expenditures), which will be addressed in future research.

CRediT authorship contribution statement

D.M. Fouz: Conceptualization, Methodology, Investigation, Formal analysis, Visualization, Writing – original draft. **R. Carballo:** Conceptualization, Methodology, Writing – review & editing, Supervision, Project administration, Funding acquisition. **I. López:** Formal analysis, Visualization, Writing – review & editing, Supervision. **G. Iglesias:** Conceptualization, Methodology, Writing – review & editing, Supervision.

Declaration of competing interest

The authors declare that they have no known competing financial interests or personal relationships that could have appeared to influence the work reported in this paper.

Acknowledgements

This work was funded by the PORTOS project co-financed by the Interreg Atlantic Area Programme through the European Regional Development Fund [grant number EAPA_784/2018] and 'Axudas para a consolidación e estruturación de unidades de investigación competitivas nas universidades do Sistema Universitario Galego (2020-22)' with reference number ED341B 2020/25.

The authors are also grateful for the support of Science Foundation Ireland and MaREI, the Marine Renewable Energy Centre of Ireland, grant SFI MAREI2_12/RC/2302/P2 Platform RA1b.

During this work I. López was supported by a postdoctoral grant of the 'Programa de Axudas á etapa posdoutoral da Xunta de Galicia' with reference number ED481D 2019/019.

References

[1] G. Agrawal, D. Mohan, H. Rahman, Ambient Air Pollution in Selected Small Cities in India: Observed Trends and Future Challenges, IATSS Research, 2021.
[2] Y. Kazancoglu, M. Ozbiltekin-Pala, Y.D. Ozkan-Ozen, Prediction and evaluation of greenhouse gas emissions for sustainable road transport within Europe, Sustainable Cities and Society 70 (2021) 102924.
[3] A.J. Njoh, Renewable energy as a determinant of inter-country differentials in CO2 emissions in Africa, Renewable Energy 172 (2021) 1225–1232.
[4] M. Zhai, G. Huang, L. Liu, B. Zheng, Y. Li, Economic modeling of national energy, water and air pollution nexus in China under changing climate conditions, Renewable Energy 170 (2021) 375–386.
[5] G. Lonati, S. Cernuschi, S. Sidi, Air quality impact assessment of at-berth ship emissions: case-study for the project of a new freight port, Sci Total Environ 409 (2010) 192–200.
[6] D. Bailey, G. Solomon, Pollution prevention at ports: clearing the air, Environ Impact Assess Rev 24 (2004) 749–774.
[7] E. Bachvarova, T. Spasova, J. Marinski, Air pollution and specific meteorological conditions at the adjacent areas of sea ports, IFAC-PapersOnLine 51 (2018) 378–383.
[8] A.M. Kotrikla, T. Lilas, N. Nikitakos, Abatement of air pollution at an aegean island port utilizing shore side electricity and renewable energy, Mar Policy 75 (2017) 238–248.
[9] T. Cabral, D. Clemente, P. Rosa-Santos, F. Taveira-Pinto, T. Morais, F. Belga, et al., Performance assessment of a hybrid wave energy converter integrated into a harbor breakwater, Energies 13 (2020).
[10] I. López, R. Carballo, D.M. Fouz, G. Iglesias, Design selection and geometry in OWC wave energy converters for performance, Energies 14 (2021).
[11] F. Taveira-Pinto, P. Rosa-Santos, T. Fazeres-Ferradosa, Marine renewable energy, Renewable Energy 150 (2020) 1160–1164.
[12] P. Rosa-Santos, F. Taveira-Pinto, C.A. Rodríguez, V. Ramos, M. López, The CECO wave energy converter: recent developments, Renewable Energy 139 (2019) 368–384.
[13] E. Dallavalle, M. Cipolletta, V.C. Moreno, V. Cozzani, B. Zanuttigh, Towards Green Transition of Touristic Islands through Hybrid Renewable Energy Systems. A Case Study in Tenerife, Canary Islands, Renewable Energy, 2021.
[14] M. López, N. Rodríguez, G. Iglesias, Combined floating offshore wind and solar PV, Journal of Marine Science and Engineering 8 (2020).
[15] C. Perez-Collazo, R. Pemberton, D. Greaves, G. Iglesias, Monopile-mounted wave energy converter for a hybrid wind-wave system, Energy Conversion and Management 199 (2019) 111971.
[16] I. Iglesias, A. Bio, L. Bastos, P. Avilez-Valente, Estuarine hydrodynamic patterns and hydrokinetic energy production: the Douro estuary case study, Energy 222 (2021) 119972.
[17] D.M. Fouz, R. Carballo, V. Ramos, G. Iglesias, Hydrokinetic energy exploitation under combined river and tidal flow, Renewable Energy 143 (2019) 558–568.
[18] Z. Yang, T. Wang, R. Branch, Z. Xiao, M. Deb, Tidal stream energy resource characterization in the Salish Sea, Renewable Energy 172 (2021) 188–208.
[19] M. Lewis, R. O'Hara Murray, S. Fredriksson, J. Maskell, A. de Fockert, S.P. Neill, et al., A standardised tidal-stream power curve, optimised for the global resource, Renewable Energy 170 (2021) 1308–1323.
[20] M. Thiébaut, A. Sentchev, Tidal stream resource assessment in the Dover Strait (eastern English Channel), International Journal of Marine Energy 16 (2016) 262–278.
[21] G. Pinon, P. Mycek, G. Germain, E. Rivoalen, Numerical simulation of the wake of marine current turbines with a particle method, Renewable Energy 46 (2012) 111–126.
[22] D. Fallon, M. Hartnett, A. Olbert, S. Nash, The effects of array configuration on the hydro-environmental impacts of tidal turbines, Renewable Energy 64 (2014) 10–25.
[23] D.T. Pugh, Tides, Surges, and Mean Sea-Level/a Handbook for Engineers and Scientists, John Wiley & Sons Inc, 1996.
[24] T.L. Sheehan, M.G. Healy, Sub-recent changes in annual average water level in the Shannon estuary, Western Ireland, J Coast Res (2006) 193–197.
[25] M. Álvarez, R. Carballo, V. Ramos, G. Iglesias, An integrated approach for the planning of dredging operations in estuaries, Ocean Engineering 140 (2017) 73–83.
[26] G. Iglesias, R. Carballo, Seasonality of the circulation in the Ría de Muros (NW Spain), J Mar Syst 78 (2009) 94–108.
[27] G. Iglesias, M. Sánchez, R. Carballo, H. Fernández, The TSE index – a new tool for selecting tidal stream sites in depth-limited regions, Renewable Energy 48 (2012) 350–357.
[28] R. Carballo, G. Iglesias, A. Castro, Residual circulation in the Ría de Muros (NW Spain): a 3D numerical model study, J Mar Syst 75 (2009) 130.
[29] G. Iglesias, R. Carballo, Effects of high winds on the circulation of the using a mixed open boundary condition: the Ría de Muros, Spain, Environmental Modelling & Software 25 (2010) 455–466.
[30] L.S. Blunden, A.S. Bahaj, Initial evaluation of tidal stream energy resources at Portland Bill, UK, Renewable Energy 31 (2006) 121–132.
[31] R. Carballo, G. Iglesias, A. Castro, Numerical model evaluation of tidal stream energy resources in the Ría de Muros (NW Spain), Renewable Energy 34 (2009) 1517–1524.
[32] V. Ramos, G. Iglesias, Performance assessment of tidal stream turbines: a parametric approach, Energy Conversion and Management 69 (2013) 49–57.
[33] C.J. Mejia-Olivares, I.D. Haigh, N.C. Wells, D.S. Coles, M.J. Lewis, S.P. Neill, Tidal-stream energy resource characterization for the Gulf of California, México. Energy 156 (2018) 481–491.
[34] Deltares User, Manual Delft3D-FLOW, Deltares ed., 2010. Delft, The Netherlands.
[35] R. O'Toole, M. Judge, F. Sacchetti, T. Furey, E. Mac Craith, K. Sheehan, et al., Mapping Ireland's coastal, shelf and deep-water environments using illustrative case studies to highlight the impact of seabed mapping on the generation of blue knowledge, Geological Society, London, Special Publications 505 (2020) SP505–2019-2207.
[36] C. Souto, M. Gilcoto, L. Fariña-Busto, F.F. Pérez, Modeling the residual circulation of a coastal embayment affected by wind-driven upwelling: circulation of the Ría de Vigo (NW Spain), Journal of Geophysical Research 108 (4–1) (2003) 4–18.
[37] S. Torres López, R.A. Varela, E. Delhez, Residual circulation and thermohaline distribution of the Ría de Vigo: a 3-D hydrodynamic model, Scientia Marina 65 (2001) 277–289.
[38] C. Le Provost, A.F. Bennett, D.E. Cartwright, Ocean tides for and from topex/poseidon, Science 267 (1995) 639–647.
[39] G.D. Egbert, A.F. Bennett, M.G.G. Foreman, Topex/Poseidon tides estimated using a global inverse model, Journal of Geophysical Research 99 (1994) 24821–24852.
[40] G. Iglesias, R. Carballo, A. Castro, Baroclinic modelling and analysis of tide- and wind-induced circulation in the Ría de Muros (NW Spain), J Mar Syst 74 (2008) 475–484.
[41] J.P. Sánchez-Úbeda, M.L. Calvache, C. Duque, M. López-Chicano, Filtering methods in tidal-affected groundwater head measurements: application of harmonic analysis and continuous wavelet transform, Advances in Water Resources 97 (2016) 52–72.
[42] V. Ramos, R. Carballo, M. Álvarez, M. Sánchez, G. Iglesias, A port towards energy self-sufficiency using tidal stream power, Energy 71 (2014) 432–444.
[43] V. Ramos, R. Carballo, M. Álvarez, M. Sánchez, G. Iglesias, Assessment of the impacts of tidal stream energy through high-resolution numerical modeling, Energy 61 (2013) 541–554.
[44] O'Carroll JPJ, R.M. Kennedy, A. Creech, G. Savidge, Tidal Energy: the benthic effects of an operational tidal stream turbine, Mar Environ Res 129 (2017) 277–290.
[45] R. Joy, J.D. Wood, C.E. Sparling, D.J. Tollit, A.E. Copping, B.J. McConnell, Empirical measures of harbor seal behavior and avoidance of an operational tidal turbine, Mar Pollut Bull 136 (2018) 92–106.
[46] P. Qian, B. Feng, H. Liu, X. Tian, Y. Si, D. Zhang, Review on configuration and

control methods of tidal current turbines, Renewable and Sustainable Energy Reviews 108 (2019) 125–139.
[47] L. Castro-Santos, M.I. Lamas-Galdo, A. Filgueira-Vizoso, Managing the oceans: site selection of a floating offshore wind farm based on GIS spatial analysis, Marine Policy 113 (2020) 103803.
[48] L. Castro-Santos, G.P. Garcia, T. Simões, A. Estanqueiro, Planning of the Installation of Offshore Renewable Energies: a GIS Approach of the Portuguese Roadmap, Renewable Energy, 2018.
[49] European Comission, The Exploitation of Tidal Marine Currents, Report EUR16683EN, 1996.
[50] I.P.L. Technomare SpA, Non Nuclear Energy – JOULE II. Wave Energy Project Results. The Exploitation of Tidal Marine Currents, EU JOULE contract JOU2-CT94-0355, 1996.
[51] K.E. Dyer, Estuaries: A Physical Introduction, John Wiley, New York, 1997.